Supersonic Inflatable Aerodynamic Decelerators For Use On Future Robotic Missions to Mars

Ian G. Clark, Allison L. Hutchings, Christopher L. Tanner, Robert D. Braun
Guggenheim School of Aerospace Engineering
Georgia Institute of Technology
Atlanta, GA 30332-0150
ian.clark@gatech.edu

Abstract—The 2009 Mars Science Laboratory mission is being designed to place an 850 kg rover on the surface of Mars at an altitude of at least one kilometer [1]. This is being accomplished using the largest aeroshell and supersonic parachute ever flown on a Mars mission. Future missions seeking to place more massive payloads on the surface will be constrained by aeroshell size and deployment limitations of supersonic parachutes [2],[3]. Inflatable aerodynamic decelerators (IADs) represent a technology path that can relax those constraints and provide a sizeable increase in landed mass. This mass increase results from improved aerodynamic characteristics that allow IADs to be deployed at higher Mach numbers and dynamic pressures than can be achieved by current supersonic parachute technology.

During the late 1960's and early 1970's preliminary development work on IADs was performed. This included initial theoretical shape and structural analysis for a variety of configurations as well as wind tunnel and atmospheric flight tests for a particular configuration, the Attached Inflatable Decelerator (AID). More recently, the Program to Advance Inflatable Decelerators for Atmospheric Entry (PAI-DAE) has been working to mature a second configuration, the supersonic tension cone decelerator, for use during atmospheric entry. [1,2]

This paper presents an analysis of the potential advantages of using a supersonic IAD on a proposed 2016 Mars mission. Conclusions drawn are applicable to both the Astrobiology Field Laboratory and Mars Sample Return mission concepts. Two IAD configurations, the AID and tension cone, are sized and traded against their system-level performance impact. Analysis includes preliminary aerodynamic drag estimates for the different configurations, trajectory advantages provided by the IADs, and preliminary geometric and mass estimates for the IAD subsystems. Entry systems utilizing IADs are compared against a traditional parachute system as well as a system employing an IAD in the supersonic regime and a parachute in the subsonic regime. Key sensitivities in IAD design are included to highlight areas of importance in future technology development programs.

TABLE OF CONTENTS

1. INTRODUCTION

Towards the end of the 1960's, NASA began several technology development programs aimed at maturing deceleration technologies for use in thin-atmosphere entries. Research into entry body shapes and supersonic parachutes was undertaken with the objective of enabling the successful landing of a spacecraft on the surface of Mars. Although the initial beneficiaries of these efforts were the two 590 kg Viking landers, the developed technologies became the foundation for every subsequent Mars entry vehicle. Over the past 30 years incremental improvements in aeroshell and parachute technologies have allowed for a gradual increase in Mars landed mass. However, these improvements are rapidly reaching their limits. The latest mission in development, the 2009 Mars Science Laboratory (MSL), is being designed to land an 850 kg rover at an altitude of at least one kilometer [1]. To do this, MSL will require the largest diameter aeroshell (4.5 m) and the largest diameter supersonic parachute (21.5 m) ever flown on Mars (see Table 1). Furthermore, parachute deployment is planned at a higher Mach number (2.2) and dynamic pressure (750 Pa) [4] than on any previous Mars mission. This system may be near the limits of current parachute technology [2] and later missions attempting marginal increases in landed mass will be faced with a difficult decision: either attempt to extrapolate current decelerator technology further beyond the tested and validated flight regime, or invest in a new, costly technology development program.

[1] 1-4244-1488-1/08/$25.00 ©2008 IEEE.
[2] IEEEAC paper#1419, Version 3, Updated 2007:12:14

Table 1. Supersonic DGB dimensions and nominal deployment conditions.

Mission	Diam. (m)	Area (m^2)	Deploy Mach	Deploy Q (Pa)	Landed Mass (kg)
Viking I	16.0	201.1	1.1	350	612
Viking II	16.0	201.1	1.1	350	612
MPF	12.5	122.7	1.57	585	370
MER-A	14.0	153.9	1.77	725	539
MER-B	14.0	153.9	1.77	750	539
Phoenix	11.7	107.5	1.2	430	364
MSL	21.5	363.1	2.2	750	850
AFL/MSR	23.0	415.5	2.3	800	~1050

One promising technology path involves the use of a supersonic inflatable aerodynamic decelerator (IAD). Often referred to as "ballutes" in the literature, IADs underwent a considerable amount of development beginning in the late 1960's [3]. This included the derivation of fundamental structural theories [5], several sets of wind tunnel tests [6], and multiple atmospheric flight tests [7] on a variety of configurations. However, since the impetus for much of the initial research was as a parallel technology path for the Viking decelerator program, development effectively ended with that program's conclusion. More recently, NASA's Program to Advance Inflatable Decelerators for Atmospheric Entry (PAI-DAE) has begun a development program aimed at maturing IADs for both human and robotic use. Areas of focus for PAI-DAE include material development, mission and system design, wind tunnel testing, and atmospheric flight testing of deployable aerodynamic decelerators.

The primary purpose of a supersonic IAD is to provide a large drag area at Mach numbers and dynamic pressures considerably higher than those presently possible using parachutes. This earlier deployment provides several distinct advantages including increased timeline for key staging events, deceleration at higher altitudes, and access to higher elevation landing sites. Although hypersonic IADs offer additional benefits in the form of reduced heating rates, supersonic IADs provide a more near-term technology solution to the problem of landing one metric ton and larger masses on the surface of Mars. Furthermore, development of supersonic IADs would set the groundwork for eventual qualification of IADs for hypersonic use.

The objective of this investigation is to quantify the potential advantages offered by a supersonic IAD with respect to a baseline robotic Mars mission. Preliminary aerodynamic and structural analyses are conducted for two separate IAD configurations. Results from these analyses are used to quantify trajectory effects and provide mass estimates for an IAD system. Finally, key sensitivities are addressed so as to provide insight into areas of further research and technology development.

2. MISSION OVERVIEW

Nominal Mission

A large rover mission in the 2016 Mars opportunity is baselined for this investigation. Such a mission may take shape through either the Astrobiology Field Laboratory (AFL) or Mars Sample Return (MSR) flight projects. Envisioned as a follow-on rover mission to MSL, a significant portion of the MSL entry, descent, and landing heritage [8] is assumed. The entry vehicle configuration, shown in Figure 1, is identical to that used by MSL. The rover mass is anticipated to be 10 - 25% higher than MSL, primarily due to accommodation of a more complex science payload [8] and increased pinpoint landing requirements. For the purposes of this study, an entry mass of 4,200 kg is assumed (31% higher than MSL). It should be noted that this value yields a packing density of approximately 195 kg/m^3, or nearly 85% of the packing density achieved with the Mars Exploration Rovers, implying a complex and difficult packaging arrangement.

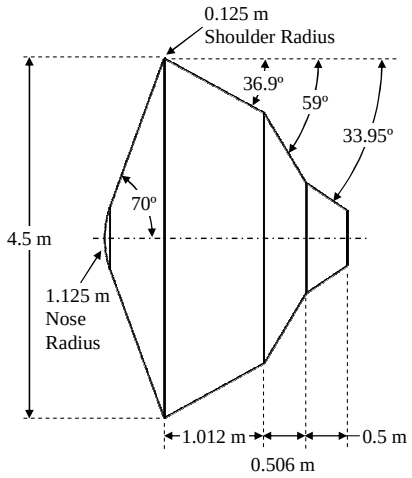

Figure 1. AFL entry capsule.

The 2016 mission entry sequence is intended to mirror MSL in many respects, including the use of a center of mass offset to provide trim at an angle of attack and subsequently an L/D of approximately 0.24. Hypersonic guidance via lift vector (bank angle) modulation is baselined to improve landing accuracy. In the present study, a reference trajectory is assumed using a reference bank-angle profile, an entry flight path angle of -16.1º, and an entry velocity of 5.2 km/sec. The resulting trajectory is shown in Figure 2.

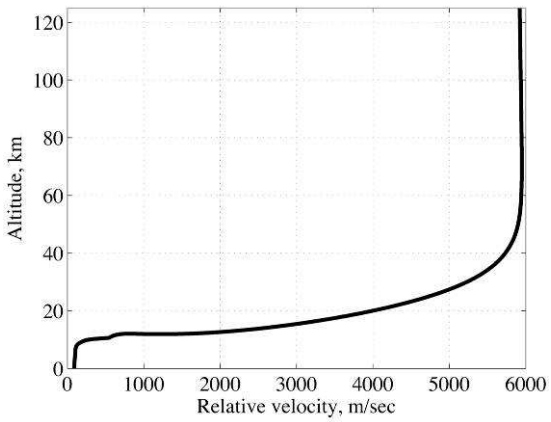

Figure 2. Reference trajectory.

For this reference trajectory, the final stages of descent assume nominal deployment of a 23 m supersonic disk-gap-band (DGB) parachute at a Mach number of 2.3 and a dynamic pressure of 800 Pa. Note that this assumed DGB parachute performance is above that planned for MSL, which itself is above that successfully demonstrated to data (see Table 1). Upon inflation, the parachute rapidly decelerates the entry vehicle through transonic and into subsonic flight conditions. As with MSL, heatshield separation is assumed to occur upon reaching a Mach number of 0.7. The terminal descent portion of flight is performed using the MSL skycrane architecture. For MSL, powered descent initiation is dependent upon ground acquisition by a terminal descent sensor followed by measurement of the vehicles altitude and velocity [1]. Although no specific set of flight conditions define the point at which the descent engines are ignited, it was assumed that the earliest this event could occur is 20 seconds after heatshield jettison. For the reference trajectory, this occurs at an altitude of 7.3 km and a velocity of 112 m/s.

IAD-Modified Mission

Two major variations to the reference mission profile are proposed. The first consists of the elimination of the DGB parachute in favor of a supersonic inflatable aerodynamic decelerator. The objective in this case is to allow for significant deceleration earlier in the trajectory and consequently allow for landing at higher elevations than would otherwise be possible using a parachute alone.

Previous robotic Mars missions have limited parachute deployment to Mach numbers less than 2.1 due to the lack of deployment and initial inflation test data obtained at the Earth in Mars relevant conditions above this Mach number and the severe area oscillations that have been observed in DGB parachutes at Mach numbers above approximately 1.5. Historical testing of supersonic IAD's has shown no area oscillation susceptibility due to Mach number effects. Thus, this analysis placed no such Mach restriction with the exception that deployment must occur at a Mach number less than 5 to allow the neglect of aerothermal heating considerations.

By design of the reference bank profile, as the entry vehicle slows to supersonic velocities, the lift vector is returned to near vertical causing a small loft in the trajectory. The IAD modified mission takes advantage of this feature by waiting until the peak loft altitude is attained before initiating deployment. Entry flight path angle variation was also performed in an attempt to position this loft at Mach numbers and altitudes larger than for the nominal trajectory.

Two-Stage IAD / Parachute Mission

Although IADs offer excellent aerodynamics in high Mach number, high dynamic pressure environments, this generally comes at the expense of a system that is more massive than a traditional parachute. Parachutes on the other hand perform very well in subsonic environments. Previous studies have shown that the optimal solution from a mass standpoint may be to incorporate a two-stage IAD-parachute system [9]. In this manner, the IAD can be deployed at high supersonic conditions, decelerate the vehicle to subsonic conditions, and then give way to a more efficient parachute system. The second alternative mission profile examines this concept by discarding the IAD at a Mach number of 0.9 and subsequently deploying a ringsail parachute.

3. DECELERATOR CONFIGURATIONS

Three types of aerodynamic decelerators are evaluated for this study: a supersonic tension cone IAD, a supersonic isotensoid IAD, and a subsonic ringsail parachute. Descriptions of each are provided below.

Tension Cone

The tension cone concept consists of a shell of revolution that is inherently shaped so as to contain only tensile stresses. The shape of the shell is derived from a prescribed pressure distribution using linear membrane theory [5]. The tension in the shell is resisted at one end by attachment to the entry vehicle and at the other end through the use of a compression ring, typically consisting of an inflated torus. A conceptual image of the tension shell as it is envisioned for this study is provided in Figure 3.

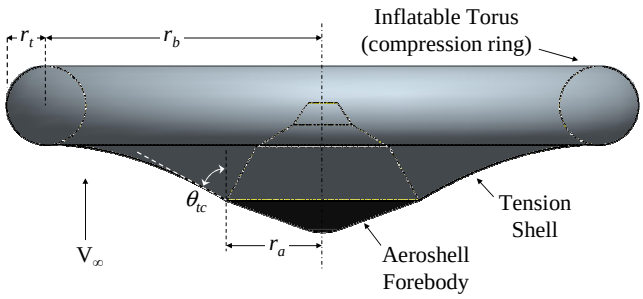

Figure 3. Tension cone configuration.

For later aerodynamic analyses a baseline tension cone configuration was established. The primary geometric parameters for the baseline tension cone are provided in Table 2. The exact shape of the tension shell portion was determined through iteration of inviscid CFD solutions. The iteration consisted of calculating an initial curvature assuming a Newtonian pressure distribution. Subsequent CFD analysis on the Newtonian derived shell provided a new pressure distribution, which in turn was used to calculate a new shell shape. Three additional iterations yielded a converged shape.

Table 2. Baseline tension cone geometry values.

Parameter	Value
Cone angle, θ_{tc}	60º
Ratio of tension cone area to aeroshell area, $(r_b+r_t)^2/r_a^2$	10
Torus radius ratio, r_b/r_t	7
r_a	2.25 m
r_b	6.225 m
r_t	0.89 m

Deployment of the tension cone occurs when the torus is rapidly pressurized using either a gas generator or pressure tank based inflation system. Detailed modeling of the inflation system and deployment dynamics are neglected for this conceptual design study.

Isotensoid IAD

The Attached Inflatable Decelerator (AID) was developed in the late 1960's by the Goodyear Aerospace Corporation to overcome flutter and stability problems encountered with supersonic parachutes. The concept consists of an aftbody decelerator that is directly attached to the aeroshell. The AID was designed using isotensoid theory [10], which provides constant tension along the decelerator's meridonal cords and uniform fabric stress in all directions throughout the surface. Designing for uniform fabric stress prevents the formation of local wrinkles along the decelerator surface (which have been shown to cause undesirable flutter and structural failure), and results in easier fabrication than other concepts with varying stress.

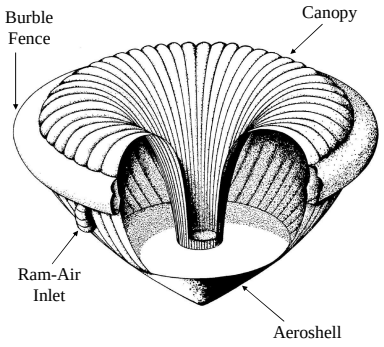

Figure 4. Illustration of AID concept [6].

The AID uses ram-air inlets, shown in Figure 4, that face in the direction of the local flow to maintain the canopy shape and create an internal pressure greater than that of the external aerodynamic pressure. Additionally, a burble fence, located at the maximum radius of the isotensoid, is employed to add aerodynamic stability at transonic and subsonic speeds. The AID utilized in this study is shown in Figure 5 with the pertinent isotensoid parameters indicated in Table 3. Similar to the tension cone, the decelerator canopy half-angle (θ') does not precisely match the aeroshell half-angle (θ) at the attach point.

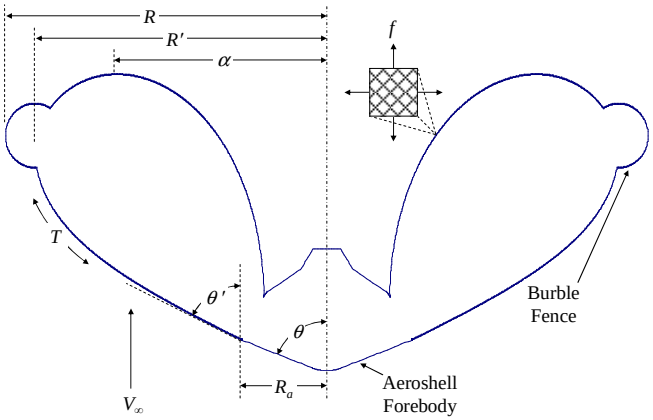

Figure 5. AID configuration schematic.

Table 3. AID parameters.

Parameter	Symbol	Dimension
Total decelerator radius	R	1.1R′
Aeroshell attach point radius	R_a	0.2985R′
Radius @ max isotensoid height	α	0.70R′
Aeroshell half-angle	θ	70 deg
Leeward fabric stress resultant	f_r	900 N/m

Inflation rate of the AID is a function of the mass flow rate into the canopy through the ram-air inlets and out of the canopy due to material porosity. These rates can be tailored by optimizing inlet area and material porosity to achieve a desired inflation rate that balances deceleration loads and inflation stability. Wind tunnel testing of the inflation process indicated inflation times on the order of 0.6 seconds for a 1.5 meter diameter device [12]. Inflation times for full scale articles are expected to be of similar order and thus inflation of the AID device is modeled as instantaneous.

Ringsail Parachute

A ringsail parachute was analyzed as a potential second-stage decelerator as it has demonstrated a high subsonic drag coefficient, good stability characteristics, and is relatively lightweight per unit drag area [11]. Additionally, the ringsail canopy can be designed for optimum performance for a given flight condition, enabling ringsail configurations to achieve subsonic drag coefficients of 0.8 or better.

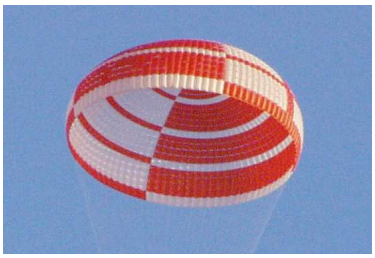

Figure 6. Deployed ringsail parachute.

Subsonic inflation of the parachute can be modeled as occurring linearly over a constant number of parachute diameters [11]. Even for a large parachute (> 20 m diameter) deploying at 100 m/s, the inflation time is less than two seconds; thus in this analysis, the ringsail parachute inflation is also modeled as occurring instantaneously.

4. AERODYNAMICS

A moderate amount of wind tunnel testing of the two IAD configurations was performed in the 1960's [6]. This included evaluation of the deployment behavior of several isotensoid models as well as static aerodynamic characterization of the isotensoid and tension cone concepts.

Results from isotensoid deployment tests demonstrated favorable behavior including the lack of any flutter characteristics [12]. Additionally, the isotensoid shape did not exhibit shock loads commonly observed in parachute deployments. Possible explanations for this include the lack of an apparent mass effect and the ram-air inflation mechanism providing a more controlled deployment. Drag coefficients measured at supersonic conditions were typically between 1.1 and 1.2, though models tested without the burble fence provided slightly higher values of about 1.4. Drag was observed to vary little with minor variations in angle of attack and Reynolds Number [12].

Testing of multiple rigid tension cone configurations yielded drag coefficients between 1.3 and 1.6 depending upon cone angle (θ_{tc}), nose radius, and shoulder radius (R_t). Of particular interest due to aerothermal and stability concerns was the presence of embedded shocks on the tension shell depending upon the cone angle. In particular, shallower cone angles and moderate cone angles at an angle of attack demonstrated embedded shocks [13].

An aerodynamic assessment of the two IAD configurations was performed for the purpose of establishing an approximate aerodynamic dataset for trajectory modeling. Using the wind tunnel data as a source of validation, a computational analysis of the baseline geometries was performed. NASCART-GT, a Cartesian-grid based CFD code [14], was used to analyze the baseline IAD configurations. Cases were run at 0° angle of attack across a range of nominal trajectory points to provide profiles of drag coefficient as a function of Mach number. Supersonic cases assumed inviscid aerodynamics, and demonstrated good agreement with wind tunnel data. Transonic and subsonic cases were run using Navier-Stokes methods employing a k-epsilon turbulence model.

Sample results from the analysis are shown in Figure 7 and Figure 8. In the case of the tension cone, the CFD analysis confirmed that the 60º cone angle was sufficient to prevent the formation of an embedded shock on the tension shell surface. However, the isotensoid configuration exhibited a weak shock forming just in front of the burble fence. Although no Schlieren imagery is available from the wind tunnel tests of the isotensoid, it is expected that an embedded shock likely existed in those tests as well. Video imagery from some of those tests showed no detrimental impact on the IAD or the burble fence due to flow separation behind the embedded shock.

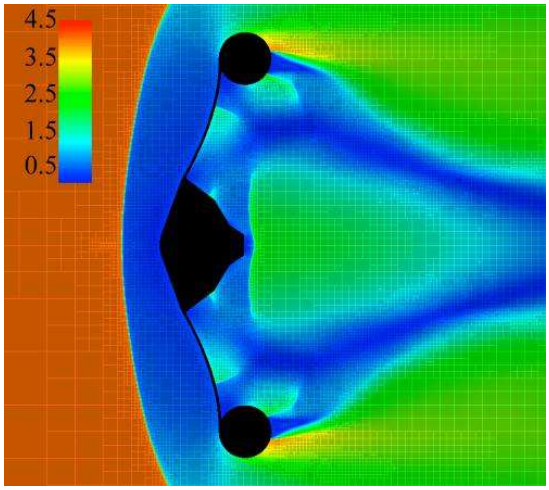

Figure 7. Inviscid Mach number profile for the baseline tension cone configuration at Mach 4.5.

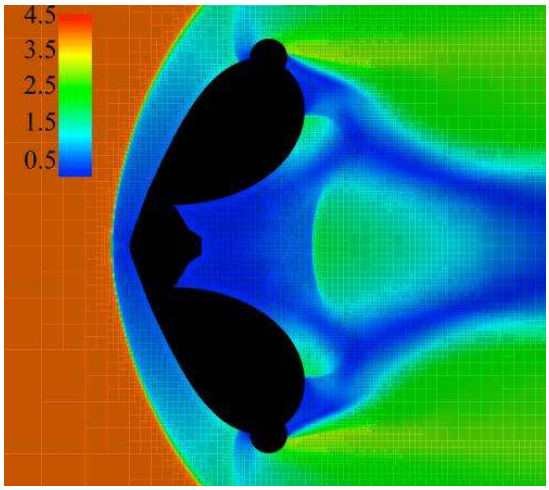

Figure 8. Inviscid Mach number profile for the baseline isotensoid configuration at Mach 4.5.

The computational aerodynamic analysis was compiled into a preliminary aerodynamic database of the two baseline IAD configurations. These results are shown in Figure 9. From

the results it can be seen that the tension cone offers similar drag performance to a rigid 60º or 70º sphere cone while the isotensoid configuration provides roughly 20% less drag. Both configurations offer 2-3 times the supersonic drag of a DGB parachute, with this advantage decreasing to ~25% at subsonic conditions. Furthermore, neither IAD configuration exhibits the transonic drag bucket common to parachutes and other decelerators which trail an entry system. The lack of a drag bucket may allow for the heatshield to be discarded much earlier in the trajectory as recontact with the entry vehicle is less likely.

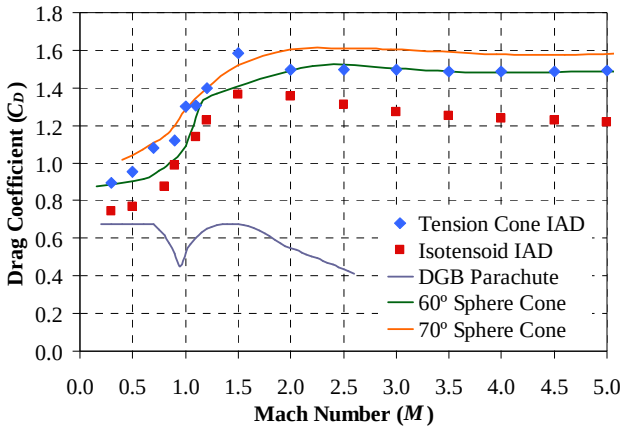

Figure 9. Comparison of drag coefficient as a function of Mach number for IADs, sphere cone aeroshells, and parachutes.

4. STRUCTURAL ANALYSIS

Neither the tension cone nor isotensoid decelerators have been fabricated at scales comparable to flight-like devices. Thus, many uncertainties exist about the exact nature in which these articles would be fabricated. These uncertainties in turn make mass estimation difficult. For this study an approach was utilized in which basic structural principles were combined with tension cone and isotensoid shape theory. The result is a preliminary estimate of the loads and stresses encountered by the two supersonic IADs. This in turn is combined with assumed material properties to derive thickness estimates and subsequently material mass estimates. A summary of the structural considerations incorporated in the analysis is provided below.

Tension Cone Structural Analysis

The inflatable tension cone consists of two elements, the tension shell and the inflated torus. The tension shell provides a majority of the drag area while the torus is used to resist the loading of the tension shell. The meridional stress resultant $N_{\phi,ts}$, expressed in Equation 1, is a function of the drag felt by the shell (D_{ts}) and the torus (D_t), the shell attachment angle (ϕ_a), and the aeroshell radius (r_a) [5].

$$N_{\phi,ts} = \frac{D_t + D_{ts}}{2\pi r_a \sin\phi_a} \tag{1}$$

The key structural constraint for the tension shell is that the meridional stress ($\sigma_{\phi,ts}$) does not exceed the yield strength of the shell material such that

$$\sigma_{\phi,ts} = \frac{N_{\phi,ts}}{t_{ts}} \le \sigma_{\phi,ts}^{\max} \tag{2}$$

where t_{ts} is the thickness of the tension shell material. The use of Equations 1 and 2 allow for an estimate of the required shell thickness as a function of the allowable material stress ($\sigma_{\phi,ts}^{\max}$).

The primary sources of stress on the inflatable torus originate from the tension shell loading and the internal pressure required to resist that loading. Five design constraints were identified for the torus, three stress based criteria and two planar buckling criteria. These include:

(a) The compressive meridional stress on the torus must be less than the maximum material strength ($\sigma_{\phi,t}^{\max}$),

$$\sigma_{\phi,t} = -\frac{r_b N_o}{\pi r_t t_t} \le \sigma_{\phi,t}^{\max} \tag{3}$$

where r_t and r_b are defined in Figure 3, t_t is the thickness of the torus material, and N_0 is the meridional stress resultant N_ϕ evaluated at r_b.

(b) The inflation pressure must be sufficient to prevent local wrinkling on the torus walls from the compressive stress.

$$p_t \ge \frac{2 r_b N_o}{\pi r_t^2} \tag{4}$$

(c) The torus stress in the circumferential direction (σ_{θ,P_t}) must not exceed material limits [15].

$$\sigma_{\theta,p_t} = \frac{p_t r_t}{2t_t}\frac{2r_b - r_t}{r_b - r_t} \le \sigma_{\theta,p_t}^{\max} \tag{5}$$

(d) The applied hoop force due to the tension shell loading (P) must be lower that the force needed to induce *in-plane* buckling [16][17],

$$P_{cr,i} = \frac{4.5EI}{r_b^2}\left(1 + \frac{3}{2}c + \frac{4 + 4.5c}{S + P^*}\right)^{-1} \tag{6}$$

$$P = \frac{D_{ts}}{\cos\phi_a} \le P_{cr,i} \tag{7}$$

where E is the material's modulus of elasticity and I is the torus inertia tensor. The parameters c, S, and P^* are shear stiffness, toroid slenderness, and pressure stiffness parameters defined in [16].

(e) The applied force due to the tension shell loading must be lower that the force needed to induce *out-of-plane* buckling [16][17],

$$P_{cr,o} = \frac{EI}{r_b^2}\left(12+\frac{3}{2}\frac{\Gamma}{S+P^*}\right)\left[4+5c+\frac{1}{\Gamma}\left(1+\frac{20}{3}c\right)+\frac{1}{S+P^*}\left(\frac{99}{8}+\frac{111}{8}c\right)+\frac{\Gamma}{S+P^*}\left(\frac{1}{2}+\frac{5}{6}c\right)\right]^{-1} \tag{8}$$

$$P = \frac{D_{ts}}{\cos\phi_a} \le P_{cr,o} \tag{9}$$

where Γ is a buckling load parameter defined in [16].

A major assumption inherent in the above formulations is that the torus wall is a membrane structure in that the local bending stiffness of the torus walls is neglected. This has particular implications in the determination of the required inflation pressure p_t and in the two buckling modes. Torus construction methods that provide additional stiffness other than that due to pressurization would likely reduce pressure requirements and provide additional torus buckling margin.

Isotensoid Structural Analysis

Isotensoid design is based on equal principle forces in the fabric between meridians, which are constant over the canopy surface. Additionally, the tension in each meridian is constant over its entire length. For AID design, these principles hold except that the fabric stress and meridional tension is higher on the windward side due to the concentrated load of the burble fence at the canopy equator. The non-dimensional fabric stress $\left(\bar{f}\right)$ and meridional tension $\left(\overline{T}\right)$ coefficients are given by Equation 10. The fabric stress is related to the meridional tension through geometry of the isotensoid via Equation 11.

$$\bar{f} = \frac{2f}{p_\tau R'} \qquad \overline{T} = \frac{nT}{p_\tau \pi R'^2} \tag{10}$$

$$\bar{f} + \overline{T} = 1-\alpha^2 \tag{11}$$

where f is the fabric stress resultant (in force per unit length), T is the meridional tension load, p_τ is the internal pressure minus the base pressure, R' is the equatorial radius of the isotensoid, n is the number of meridional cords, and α is a non-dimensional parameter that defines the radius of maximum canopy height.

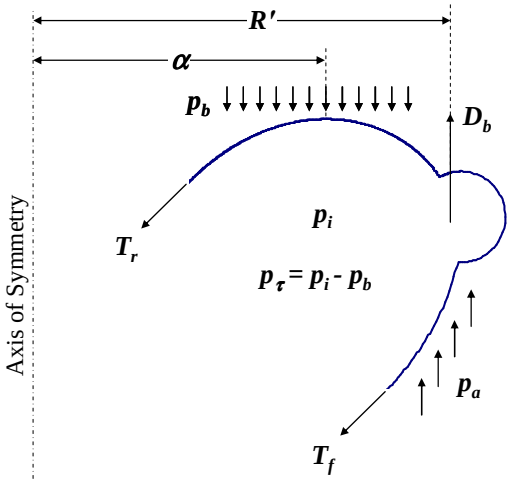

Figure 10. AID structural parameters.

The windward fabric stress and meridonal tension coefficients are assumed to take a fraction (γ) of the burble fence load in addition to the leeward loading.

$$\bar{f}_f = \bar{f}_r + \gamma\overline{N}_b \qquad \overline{T}_f = \overline{T}_r + (1-\gamma)\overline{N}_b \tag{12}$$

$$\overline{N}_b = \frac{D_b}{p_\tau \pi R'^2} \tag{13}$$

$$\gamma = \frac{\bar{f}_r}{1-\alpha^2} \tag{14}$$

where f and r subscripts represent the front (windward) and rear (leeward) components, $\overline{N}_b$ is the non-dimensional burble fence load, and D_b is the burble fence load. From these structural parameters and a choice of meridian and canopy materials, the shape [12] and mass of the isotensoid can be estimated.

5. TRAJECTORY ANALYSIS

A key advantage of an IAD is its ability to increase drag area (C_DA) earlier in the descent profile, enabling deceleration at higher altitudes versus the traditional DGB parachute. Additionally, the lack of a transonic drag bucket may permit the entry vehicle to release its heatshield at any point after IAD inflation without risking recontact. Early heatshield separation reduces the mass being decelerated and allows for onboard altimeters to acquire the ground

sooner. This latter capability allows for the initiation of propulsive descent at a higher altitude, enabling landing at higher altitudes and/or more time to perform pinpoint landing guidance.

Trajectory simulations were performed using the Program to Optimize Simulated Trajectories (POST) [16]. The entry phase up to decelerator deployment employed the same reference bank-angle profile to be consistent with the DGB reference trajectory shown in Figure 2. Three primary trades were evaluated: replacement of the nominal 23 m DGB with a supersonic IAD, replacement of the DGB with a two stage IAD-ringsail combination, and the impact of an additional 20% increase in entry system mass.

IAD and Baseline DGB System Comparison

This portion of the study investigates the system impact of increasing IAD diameters versus the present AFL baseline 23 m DGB parachute. Both IAD concepts are assessed. An initial comparison of the trajectories is provided in Figure 11, where IADs of varying diameters are shown deployed at the loft peak of the reference trajectory. Evident in Figure 11 is the rapid, constant-altitude deceleration that occurs after IAD deployment. This is followed by transition to an asymptotic terminal descent in which drag and gravitational forces are nearly equal and opposite and the vehicle is descending on a line of constant dynamic pressure. Terminal velocity is strongly dependent on the diameter of the IAD, with diameters between 14 and 23 meters shown in Figure 11. Given that the terminal velocity represents the velocity at which the entry vehicle stages to propulsive terminal descent, a trade between IAD size and propellant mass arises. For example, a 14 m tension cone IAD provides a terminal velocity of 150 m/sec at an altitude of 5 km, whereas a 20 m tension cone IAD provides a terminal velocity of 105 m/sec at the same altitude. For reference, a 23 m DGB parachute deployed at Mach 2.3 results in a terminal velocity of 100 m/sec at 5 km altitude. Clearly, a larger IAD reduces the velocity and thus the propellant required for terminal descent, though at the expense of a heavier IAD system.

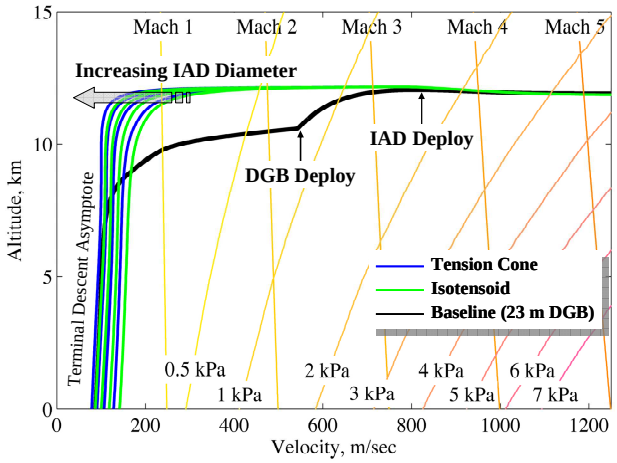

Figure 11. Comparison of reference trajectory and IAD-modified trajectories against contours of Mach and dynamic pressure (γ_{entry} = -16.1°).

Figure 11 demonstrates that a significant increase in altitude (approximately 3 km) at subsonic velocities is possible with use of an IAD. Architecturally, this altitude increase can be used to provide either an increase in terminal descent timeline or the ability to land at higher surface elevations. However, this advantage belies the greater impact that an IAD can provide as a result of its large deployment condition envelope. That is, the DGB reference trajectory places the loft peak at a Mach number of about 3.3 and dynamic pressure of 1.5 kPa, whereas a supersonic IAD is capable of deploying at higher Mach numbers and greater dynamic pressures. Thus, a more suitable comparison can be made when the loft is repositioned. Retaining the reference bank-profile, this is accomplished by entering at a shallower flight path angle. For a relative entry flight path angle of approximately -13.7° the loft peak occurs at Mach 5 and at a dynamic pressure nearly equivalent to before. The resulting trajectories are shown in Figure 12.

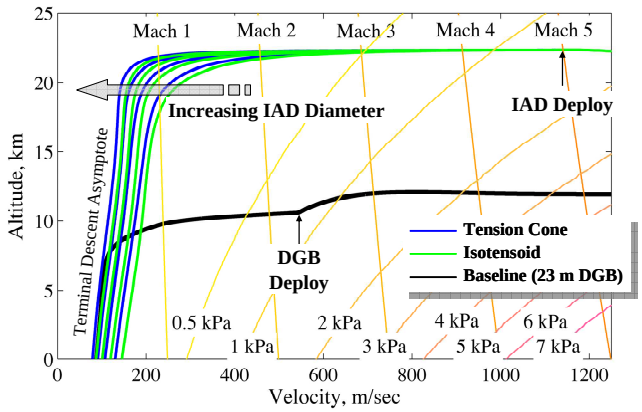

Figure 12. Trajectory comparison for IAD-modified trajectory with repositioned loft peak (γ_{entry} = -13.7°).

Of note is that even moderately sized (14 m diameter) IADs can be used to attain subsonic velocities at altitudes nearly 10 km higher than the baseline DGB trajectory. The improved drag performance of the tension cone provides

additional, but modest, advantages in altitude over the isotensoid design.

Although these trajectories do not represent optimized bank profiles they still demonstrate the expanded EDL system performance range that an IAD enables. If a steeper entry is desired, IADs can still provide a considerable altitude advantage. An example of this scenario is provided in Figure 13, where the bank profile was adjusted to provide more lift throughout the entry and the relative entry angle was steepened to -19°. This trajectory provides 8-10 km in increased altitude (as measured at the Mach 1 condition).

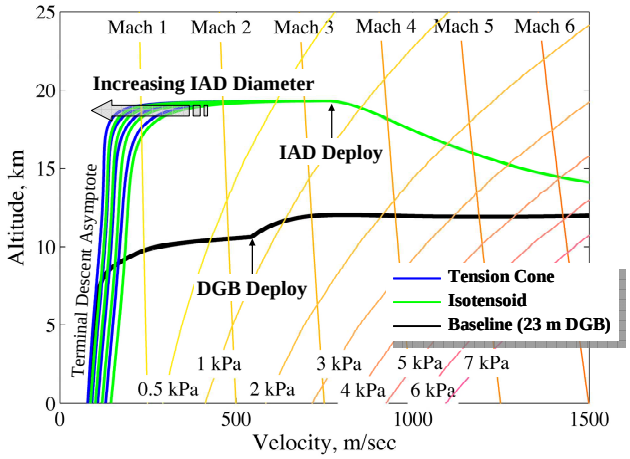

Figure 13. Trajectory comparison for steepened, lift up entry (γ_{entry} = -19°).

IAD and Two-stage System Comparisons

Use of an IAD clearly provides significant flexibility in terminal descent altitude and timeline; however a more massive IAD is required to achieve the same terminal velocity as a DGB parachute. Coupling a smaller IAD with a subsonic ringsail parachute would simultaneously allow for a lower terminal velocity, a lower IAD mass, and an increase in landed altitude. Although adding a second aerodynamic decelerator adds complexity to the EDL sequence of events, there could be significant mass savings which may act as a mission enabler. This portion of the study is performed with a 14 m IAD coupled with a ringsail parachute with diameters between 20 and 29 m. Ringsail deployment is assumed to occur at Mach 0.9. The results of this trajectory analysis are shown in Figure 14.

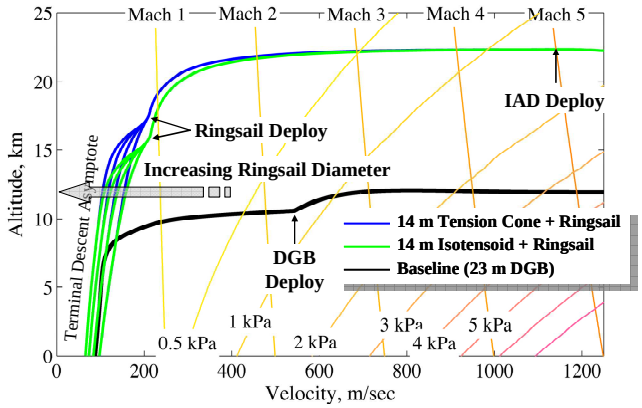

Figure 14. Hybrid trajectory comparison for various ringsail diameters (γ_{entry} = -13.7°).

Figure 14 shows a difference between the tension cone and isotensoid ringsail deployment altitude, which is expected due to the difference in drag coefficient of the two configurations. The two IAD trajectories eventually converge to the same terminal velocity given similar ringsail parachutes. With addition of the subsonic ringsail, transitioning to propulsive descent at altitudes below 10 km does not require the improved drag performance of the tension cone. Lastly, the higher drag coefficient of a ringsail parachute provides for a moderate decrease in terminal velocity versus an equivalent diameter DGB.

Entry Mass Sensitivity

To investigate the sensitivity of the inflatable decelerator and hybrid systems to increasing mass, two tension cone configurations were analyzed with two entry vehicle masses – the baseline 4.2 MT vehicle and a roughly 20% heavier 5 MT vehicle. The 5 MT entry mass corresponds to achieving the packing density of the MER vehicles within the larger 4.5 m diameter aeroshell. The results of this trajectory analysis are shown in Figure 15.

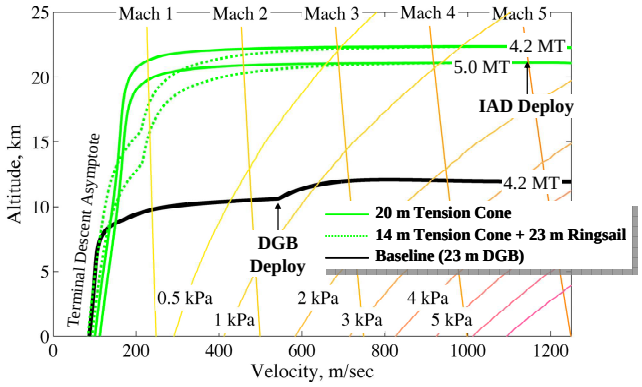

Figure 15. Trajectory comparison for two entry system masses (γ_{entry} = -13.7°).

Figure 15 shows that an increase in mass acts to lower the altitude of the loft maneuver by about 2 km and thus lower

the altitude of all subsequent EDL events. Although a decrease in altitude is undesirable, it illustrates that the tension cone is robust to entry system mass growth and still provides a significant altitude benefit versus the lower mass baseline DGB system. In addition, Figure 15 demonstrates that the two-stage 14 m tension cone IAD and ringsail system can deliver 20% more mass to approximately the same terminal velocity as the 23 m DGB reference mission.

Figure 16 shows that both the tension cone and two-stage systems undergo about a 5 km decrease in propulsive staging altitude for a 20% increase in entry mass. However, this decrease in altitude does not endanger the mission for staging velocities above 125 m/s. This staging velocity could be further reduced by baselining a larger diameter IAD or ringsail parachute.

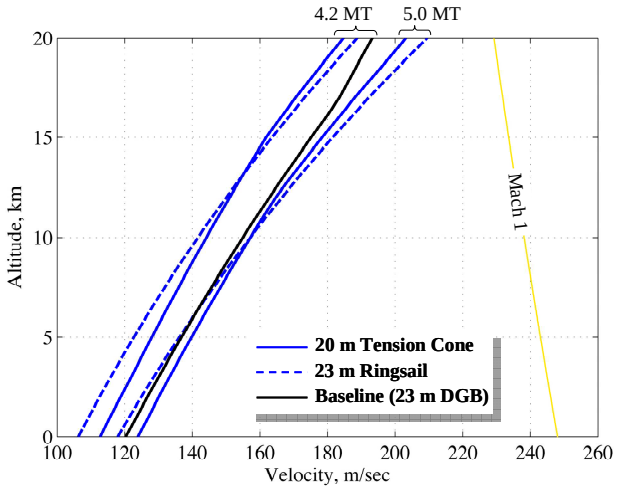

Figure 16. Staging altitudes for varying entry vehicle masses.

6. MASS ESTIMATES

The aerodynamic and trajectory benefits of an IAD are evident but the ultimate measure of their viability must include assessment of the additional mass an IAD contributes to the EDL system and can deliver to the surface. Mass estimates were obtained for all aerodynamic decelerators (parachutes and IADs) based on fundamental structural principles and historical regressions (where data is available). For both IAD configurations, the fabric or film portions of the decelerator were sized assuming the material properties of Vectran. Vectran was selected based on its high strength-to-weight ratio, good thermal performance, and heritage on the Pathfinder and Mars Exploration Rover (MER) airbags. The same 200 denier Vectran material [20] used on the two MER landers was used in this study. This material has an areal mass density (d_f) of 0.0915 kg/m^2 and a tensile strength (σ_T) of 84,940 N/m. The torus portion of the tension cone was assumed to have a higher areal density of 0.1458 kg/m^2 to account for the addition of a silicone coating used to reduce porosity. The final areal density used in mass calculations was scaled linearly with the required tensile strength of the material.

Tension Cone Mass Estimation

The mass for the tension cone was determined as a summation of four different elements: the tension shell, the torus, the inflation gas, and the inflation system. The mass of the torus and the tension shell are derived from the density of the material used, the surface area, and the required material thickness

$$m_{ts} = A_{ts}\rho_{ts}t_{ts}$$
$$m_t = A_t\rho_t t_t \quad (16)$$

where A is surface area, ρ is the material density, t is the material thickness, and the subscripts t and ts represent the torus and tension shell, respectively. The minimum thickness can be calculated by comparing the material constraints to the various modes of failure detailed in Section 4. For a coated fabric torus, the limiting case is the circumferential stress, though the required anti-wrinkling pressure and the compressive meridonal stress levels are within the same magnitude. For this limit the important parameters are the required inflation pressure, the major radius of the torus, and the torus thickness.

The mass of the inflation gas (m_{gas}) is calculated using the ideal gas law:

$$m_{gas} = \frac{p_t V_t}{RT} \quad (17)$$

where P_t is the internal torus pressure, V_t is the torus volume, R is the gas constant of the fill gas, and T is the temperature of the fill gas (assumed to be 500 K). The volume of the torus is known from geometry. Using previously detailed failure criteria the required inflation pressure can be determined. No accommodation was made in this mass estimation for pressurant gas leakage due to IAD porosity.

Both a tank system and a gas generator were investigated for the inflation system. Following the tank sizing guidelines in [16], the tank mass was estimated to be moderately higher than the mass of the inflation gas itself. Gas generators on the other hand typically yield much more favorable mass fractions. For this study a mass fraction of 75% was assumed for the gas generators.

Given the number of variables that are required to define a specific tension cone geometry it is important to understand the impact that each has on the mass and performance of the system. With this in mind an exploration of the tension cone design space was undertaken. Unless otherwise stated, the aeroshell diameter and area ratio, defined as

$$AR = \frac{(r_b + r_t)^2}{r_a^{\,2}}, \tag{18}$$

were kept constant using the values outlined in Table 2, while the ratio of r_b to r_t and the tension cone angle (θ_{tc}) were varied. The dynamic pressure at deployment, important for torus pressure and tension shell loading concerns, was kept fixed at a value of 1400 Pa. The primary measure of effectiveness was mass, along with the required inflation pressure p_t, and a decelerator-ballistic coefficient, defined as:

$$\beta = \frac{\left(m_{ts} + m_t + \frac{4}{3}m_{gas}\right)q}{D_{tot}} \tag{19}$$

The effect of θ_{tc} and the ratio of r_b to r_t on the system mass can be seen below in Figure 17.

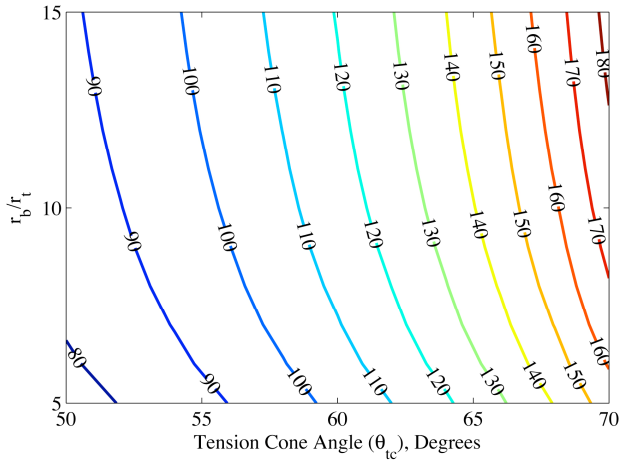

Figure 17. Mass (kg) as a function of r_b/r_t ratio and interface Angle.

The mass is seen to vary greatly with θ_{tc}, while not strongly influenced by the ratio of r_b to r_t except at the lower ratios. As the tension cone angle increases, the geometry becomes flatter, the drag increases, and the loading on the shell and torus increase as a result. Thus, the mass needed to withstand the added stresses increases. Increasing the ratio of r_b to r_t also increases the mass, but at a much lower rate. This is less intuitive as an increase in the ratio should yield a smaller torus, and less surface area. However, the decrease in torus radius drives an increase in the required inflation pressure needed to resist local surface wrinkling. This pressure increase rises more rapidly than the decrease in volume for a smaller torus. As a result, the net inflation gas mass rises. Furthermore, higher torus pressures increase the stresses on the torus and require thicker fabrics, thus raising the areal density of the material. For the material properties assumed, the inflation gas mass is shown to increase more rapidly than any decrease in material mass achieved by going to a smaller torus. The discussed change in internal pressure can be seen in Figure 18 below. Again, decreasing the torus radius, and thus increasing r_b/r_t, increases the pressure required to resist local wrinkling on the surface of the torus. Additionally, moving to larger tension cone angles increases drag and thus loading on the torus, with the results being a further increase in the required torus inflation pressure.

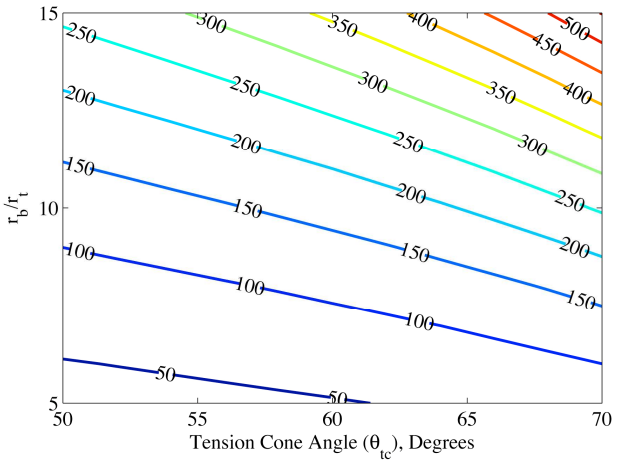

Figure 18. Inflation pressure (kPa) as a function of rb/rt and tension cone angle.

A secondary effect of changing the r_b/r_t ratio or the tension cone angle is a change in drag performance. For a fixed total diameter, increasing r_b/r_t decreases the shoulder radius and increases the drag coefficient. Likewise, decreasing the tension cone angle generates a more swept back decelerator and consequently reduces the drag coefficient. Thus, the two trends that reduce mass, namely decreasing r_b/r_t and tension cone angle, also have the effect of reducing the drag performance of the tension cone. For this reason, it is useful to examine the impact that these two variables have on the decelerator ballistic coefficient defined by Equation 19, a metric that includes both mass and drag performance. The results from this analysis are provided in Figure 19. The key result is that the ballistic coefficient follows nearly the same trend as mass, indicating the change in aerodynamics is a secondary effect.

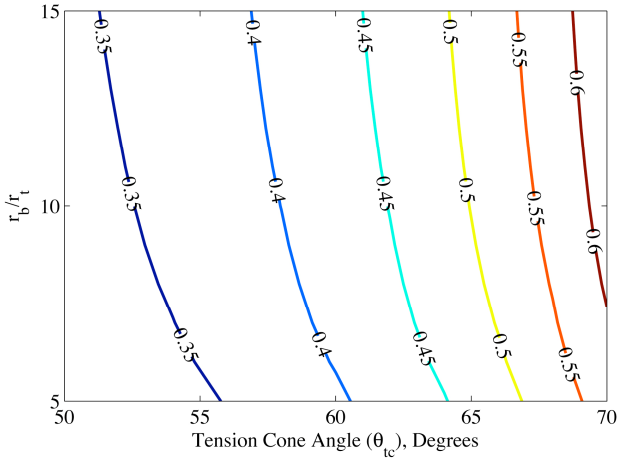

Figure 19. Decelerator ballistic coefficient (kg/m^2) as a function of rb/rt and tension cone angle.

Another important sensitivity addressed was the properties of the materials used for construction. For the level of

fidelity of this study, these are the yield stress and areal density of the fabric. The effects of varying these can be seen in Figure 20.

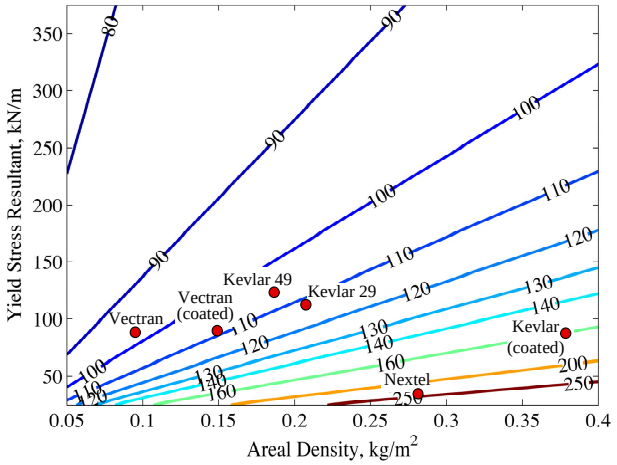

Figure 20. Mass (kg) as a function of yield strength and density.

Based upon the results of the geometry parameter sweep a tension cone angle of 60° and an r_b/r_t ratio of 7 were selected as nominal values for subsequent sizing efforts. Though not optimal, the selected tension cone angle ensures a sufficient margin against the embedded shocks mentioned in Section 3. The selected radius ratio ensures a lower mass while still providing good drag performance and lower torus volumes.

The trajectory analysis focused on IAD diameters of 14, 17, 20, and 23 m. Mass estimates for tension cones of these sizes are provided in Table 4. The results in Table 4 demonstrate that the total tension cone mass increases rapidly with increasing diameter. Furthermore, the rate of mass increase is larger than the rate of increase in the square of the total diameter. In other words, larger tension cones can be seen to yield larger decelerator ballistic coefficients.

Table 4. Tension cone mass for a range of diameters.

IAD diameter		14	17	20	23
Geometry (m)					
Tension shell radius	r_b	6.125	7.438	8.750	10.063
Torus radius	r_t	0.875	1.063	1.250	1.438
Aeroshell radius	r_a	2.25	2.25	2.25	2.25
Mass (kg)					
Tension shell	m_{ts}	2.3	5.4	11.0	19.8
Torus	m_t	29.7	55.3	92.1	142.0
Inflation gas	m_g	53.8	100.2	166.9	257.3
Gas generator	m_t	17.9	33.4	55.6	85.8
Total Mass (kg)	$\boldsymbol{m_{tc}}$	**104**	**194**	**326**	**505**

The largest contributor to the rapidly increasing mass is the inflation gas, which in turn is driven primarily by torus pressure requirements. Of the five torus design constraints identified in Section 4, it is the desire to eliminate localized wrinkling along the torus surface that affects the total mass the greatest. Should the assumption of membrane torus behavior be relaxed, and the ability of the torus to resist wrinkling be improved, the internal pressure can be reduced and dramatic improvements in total mass can be attained. This effect is shown in Table 5 below, where total tension cone masses are shown versus reduced inflation pressure requirements.

Table 5. Tension cone mass with adjusted internal pressure constraints.

IAD diameter (m)	14	17	20	23
Total mass (kg)				
100% inflation pressure	104	194	326	505
75% inflation pressure	78	147	247	384
50% inflation pressure	53	100	168	262

From Table 5 it can be seen that a 50% reduction in inflation pressure requirements provides a nearly equivalent reduction in total tension cone mass. Reducing the inflation pressure not only reduces the inflation gas mass, but also reduces the gas generator mass and the torus mass, the latter because of the reduced stresses on the torus.

Isotensoid Mass Estimation

The isotensoid mass essentially consists of two components that can be summed together – the meridional cord mass and the canopy fabric mass (assuming the canopy and burble fence are constructed of the same material). Thus, the mass of the isotensoid IAD can be represented as Equation 20 [19]

$$m_{iso} = n l_m \gamma + d_f A_s \tag{20}$$

where m_{iso} is the mass of the system, n is the number of meridional cords (assumed to be 48) of length l_m with mass per unit length γ, d_f is the material mass per unit area, and A_s is the total canopy surface area (including the burble fence). Given a desired shape, appropriate materials can be selected to satisfy the maximum fabric (f_f) and meridian stresses (T_f) required to obtain that shape.

To estimate the meridonal cord mass, a factor of safety of 5 (k_m = 5) is applied to actual meridian tension (T_{act}) to obtain the design tension (T_{design}). Given the tensile strength of Vectran, a meridian width (w_m) and subsequently a mass per unit length (γ) is determined from Equation 22. This mass per unit length is then used in Equation 20 to obtain a total meridian mass.

$$T_{design} = k_m T_{act} \tag{21}$$

$$w_m = \frac{T_{design}}{\sigma_T}$$
$$\gamma = d_f w_m \tag{22}$$

For the canopy fabric, a similar factor of safety of 5 ($k_c = 5$) is applied to the actual stress resultant to obtain a design stress resultant. The primary constraint considered is that the design stress resultant be less than the tensile strength ($\sigma_{design} \leq \sigma_T$).

A summary of the mass estimation efforts for the isotensoid is provided in Table 6. When compared to the tension cone the isotensoid is estimated as having a lower mass for a given diameter. Much of this can be attributed to the ram-air inflation mechanism of the isotensoid and the lack of a requirement for an independent inflation system. That is, even though the isotensoid configuration has significantly greater material acreage, the increase in material mass is still less than the mass of an inflation system. From a mass perspective, should it be possible to reduce the inflation pressure requirement of the tension cone torus, the two concepts would become much more equivalent. Lastly, as with the tension cone, the isotensoid can be seen to increase in mass more rapidly than the corresponding increase in drag area. However, this increase is at a lower rate than for the tension cone IAD and in general shows that the isotensoid scales better than the tension cone with regards to mass. A caveat to these results should be noted due to the lack of historical precedence in the manufacturing of IAD's at these scales. This applies equally to both the tension cone and isotensoid mass estimates.

Table 6. Isotensoid mass for a range of diameters.

IAD Diameter (m)		14	17	20	23
Meridians					
Cord Length (m)	l_m	15.7	20.7	24.5	28.7
Actual Load (N)	T_{act}	3187	4933	7152	9680
Width (m)	w_m	0.19	0.29	0.42	0.57
Meridian Mass (kg)	m_m	13.0	26.4	45.4	71.8
Canopy					
Actual Stress (N/m)	σ_{act}	1080	1080	1077	1077
Surface Area (m^2)	A_f	403	617	842	1112
Canopy Mass (kg)	m_c	36.9	56.5	77.1	101.8
Total Mass (kg)	$\boldsymbol{m_{iso}}$	**50**	**83**	**122**	**174**

Parachute Mass Estimation

Mass of the subsonic parachute system was estimated using a regression on historical ringsail system masses, resulting in the following mass estimating relationship

$$\frac{m_p}{S_0} = 0.1055\ kg/m^2 \tag{23}$$

where m_p is the parachute mass and S_0 is the parachute nominal area. The mortar mass required to eject a given parachute was similarly estimated from a linear regression of historical data, shown in Figure 21.

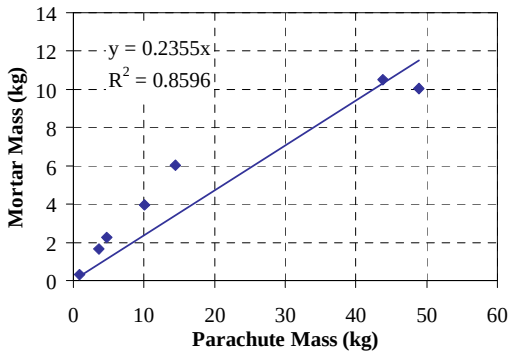

Figure 21. Mortar mass vs. parachute mass regression.

Mass Estimate Summary

A summary of the mass estimates for each decelerator combination is provided in Table 7. Of note, the smaller IADs are shown to be mass-competitive with the baseline 23 m DGB parachute.

Table 7. Mass summary of decelerator systems.

System Config	Diam. (m)	Mass (kg) IAD†	Mass (kg) Parachute*	Total
Baseline DGB	23	-	77	**77**
Tension Cone	14	104	-	**104**
	17	194	-	**194**
	20	326	-	**326**
	23	505	-	**505**
Isotensoid	14	50	-	**50**
	17	83	-	**83**
	20	122	-	**122**
	23	174	-	**174**
Tension Cone + Ringsail	14 / 20	104	41	**145**
	14 / 23	104	54	**158**
	14 / 26	104	69	**173**
	14 / 29	104	86	**190**
Isotensoid + Ringsail	14 / 20	50	41	**91**
	14 / 23	50	54	**104**
	14 / 26	50	69	**119**
	14 / 29	50	86	**136**

† IAD mass includes inflation system for tension cone
* Parachute mass includes mortar mass

Examination of mass estimates alone does not adequately portray the system view. Rather, the mass contributions must be weighed against other benefits that the IAD may provide. In particular, the trajectory benefits discussed in previous sections must also be considered. One approach taken is to consider the velocity and altitude at which the decelerator system is staged to a propulsive terminal descent system. With this approach, a mission designer can effectively say, "How large of a system do I need to be at a given altitude and velocity for staging purposes and what is the mass contribution of that system?" The following outlines the approach and results from this type of analysis.

Each decelerator system is assessed based on two metrics – the *delta* mass (Δm_{sys}) of the deceleration system (both aerodynamic and propulsive) and the altitude at which propulsive descent was initiated. The delta mass represents the change in decelerator system mass that is incurred as a result of moving to an IAD or IAD-parachute two-stage system. This delta includes the mass of the decelerator system and any additional propellant required as a result of staging at a higher velocity. The value of the delta mass is the difference between the combined IAD/ringsail/propellant mass and the baseline DGB mass.

Five velocity conditions were selected to initiate propulsive descent ranging from 200 m/s to 100 m/s (propulsive descent is initiated at 110 m/s in the DGB reference trajectory). The altitude at which these velocity conditions are achieved will depend on the size of the IAD or parachute. Since mass is a function of size (i.e. diameter), the propulsive staging altitude is directly correlated to the IAD and parachute mass. The propellant mass required to null the remaining vehicle velocity is calculated via the rocket equation

$$m_{prop} = m_i \left[1 - \exp\left(\frac{-\Delta V}{g_0 I_{sp}} \right) \right] \tag{15}$$

where m_i is the initial vehicle mass, m_f is the final vehicle mass, m_{prop} is the propellant mass, ΔV is the required change in velocity, g_0 is the acceleration due to gravity of Earth (g_0 = 9.81 m/s^2), and I_{sp} is the specific impulse of the descent rocket engines, assumed to be 205 sec based on the Viking terminal descent engines.

A summary of the delta propellant and delta system masses for each terminal velocity condition is provided in Table 8. From Table 8 it can be seen that nearly all configurations analyzed incurred mass increases over the baseline DGB system. However, the altitude at which propulsive descent can be initiated is significantly higher than the baseline configuration. For example, utilizing a 20 m isotensoid IAD and staging at 175 m/sec will incur a 150 kg increase in decelerator system mass but will also yield a 10 km increase in staging altitude. Lower staging velocities yield lower system mass increases, though at the expense of a smaller improvement in staging altitude. For example, using the same 20 m isotensoid and staging at 150 m/sec provides only a 3 km increase in staging altitude. This is due to the IAD having reached its terminal descent slope [27]. In general, higher altitudes can be achieved by staging at higher velocities. Two-stage systems that include a subsonic ringsail parachute are shown to incur lower mass increases than the single IAD system, though typically with less altitude benefit. The most favorable situation for a two-stage system is shown to be for lower propulsive staging velocities. For example, a 14 meter isotensoid coupled with a 29 meter ringsail can provide a nearly 6 km altitude increase at a staging velocity of 100 m/sec while only incurring a modest 43 kg increase in system mass.

The intent of Table 8 is to provide a mission designer with insight into the trades available for using IADs and how they may impact the descent profile. Use of a single IAD system can yield significant altitude increases so long as the vehicle is designed to stage at a higher terminal descent velocities. Staging at higher altitudes and velocities is desirable as it affords the ability to mitigate navigation errors through

Table 8. System study metric summary for 4.2 MT baseline case.

Staging Velocity (m/sec)		200		175		150		125		100	
Δm_{prop} (kg)		143		104		65		24		-16	
Configuration	**Diameter (m)**	**Staging Alt (km)**	**Δm_{sys} (kg)**	**Staging Alt (km)**	**Δm_{sys} (kg)**	**Staging Alt (km)**	**Δm_{sys} (kg)**	**Staging Alt (km)**	**Δm_{sys} (kg)**	**Staging Alt (km)**	**Δm_{sys} (kg)**
Baseline DGB	23	9.4	-	9.1	-	8.7	-	8.1	-	4.5	-
Tension Cone	14	15.9	170	10.1	131	4.7	92	-	-	-	-
	17	19.9	260	17.4	221	10.4	182	4.5	141	-	-
	20	21.1	392	20.3	353	16.9	314	9.0	273	2.8	233
	23	21.6	571	21.2	532	20.3	493	13.0	452	6.6	412
Isotensoid	14	13.0	116	6.3	77	1.0	37	-	-	-	-
	17	18.8	149	12.9	110	6.7	70	1.3	30	-	-
	20	20.7	189	19.1	150	11.7	110	5.9	70	0.1	29
	23	21.4	240	20.8	201	18.0	161	9.7	121	3.9	80
Tension Cone + Ringsail	14 / 20	15.6	211	13.8	172	10.8	133	6.3	92	0.6	52
	14 / 23	15.9	224	14.8	185	13.2	146	10.1	105	4.7	65
	14 / 26	15.9	239	15.2	200	14.2	161	12.4	120	7.9	80
	14 / 29	15.9	256	15.2	217	14.6	178	13.6	137	10.7	97
Isotensoid + Ringsail	14 / 20	14.0	157	12.5	118	10.2	78	6.3	38	0.7	-2
	14 / 23	14.2	170	13.3	131	11.9	92	9.6	51	4.7	11
	14 / 26	14.2	185	13.6	146	12.7	107	11.3	66	7.9	26
	14 / 29	14.2	202	13.6	163	13.0	123	12.1	83	10.2	43

subsonic terrain relative navigation and guidance, allows additional timeline margin for subsequent descent and landing events, and allows for landing at higher elevation sites.

Although Table 8 clearly shows altitude and trajectory advantages that can be attained from a supersonic IAD, it should also be recognized that an increase in payload mass is also attainable. Because a supersonic IAD is reasonably insensitive to increases in entry mass (Figure 15), the IAD can accommodate an entry mass increase greater than the mass of the IAD itself. For example, an entry mass of 5 MT can be decelerated to subsonic velocities at nearly the same altitude as a 4.2 MT entry mass. Since the IAD system would constitute significantly less than the 800 kg increase in mass, the net effect is an increase in payload mass. With this in mind, the mass analysis performed for the 4.2 MT entry case was also performed on a 5 MT entry case. However, the previous metric of delta system mass has been replaced with a net increase in payload capability, corresponding to the difference between the increased entry mass and the mass of the IAD and additional propellant. The results from this trade are shown in Table 9. It should be mentioned that in this context, the increased payload mass does not necessarily represent an equivalent increase in rover mass or landed mass. Rather, some of the payload increase will likely be consumed by increased structural masses, larger propellant tanks, etc. that result from an increased entry mass.

From Table 9 it can be seen that payload increases of 600 kg or more are attainable with use of an IAD system. The greatest payload increases occur with smaller IADs. For example, using a 14 m isotensoid IAD and staging at 200 m/sec can provide a 641 kg increase in payload at a staging altitude of over 9 km. Use of a parachute for this increased entry mass would require deployment at dynamic pressures of roughly 1 kPa, a full third beyond that planned for MSL. Although it may theoretically be possible to develop a parachute that would work for these increased masses, doing so would likely require a costly qualification program, similar to the Balloon Launch Decelerator Test Program undertaken for the Viking missions. Given the marginal increase in payload mass that such a program would ultimately afford, it may be more prudent to spend those resources qualifying a supersonic IAD, a technology that would enable a greater range of entry masses for future Mars systems.

7. CONCLUDING REMARKS

The objective of this system study was to show how the use of inflatable aerodynamic decelerators can provide a technology path to enable higher altitude and higher mass landing on the surface of Mars. Both a tension cone and isotensoid IAD configuration were investigated. As an aerodynamic database for such IADs does not exist, a preliminary database was constructed computationally using a cartesian flow solver. Trajectories using IADs and IAD-parachute two-stage systems were compared relative to a nominal trajectory utilizing a traditional DGB parachute.

Results from this performance analysis demonstrated the IAD ability to drastically improve the altitudes at which the entry vehicle transitioned to subsonic velocities. Additional improvement was possible when the entry flight angle or entry bank-angle reference profile was adjusted to allow for IAD deployment at higher Mach numbers and altitudes.

Structural analyses, material properties, and historical regressions were used to generate mass estimates for the decelerator systems in order to provide a complete representation of each system. These mass estimates showed the isotensoid configuration to be a lower mass solution,

Table 9. Payload increases possible for a 5 MT entry mass using various IAD configurations.

Staging Velocity (m/sec)		200		175		150		125		100	
Δm_{prop} (kg)		143		104		65		24		-16	
Configuration	**Diam. (m)**	**Stage Alt (km)**	**Δm_{pl} (kg)**	**Stage Alt (km)**	**Δm_{pl} (kg)**	**Stage Alt (km)**	**Δm_{pl} (kg)**	**Stage Alt (km)**	**Δm_{pl} (kg)**	**Stage Alt (km)**	**Δm_{pl} (kg)**
Tension Cone	14	12.7	587	7.0	638	1.7	689	-	-	-	-
	17	17.9	497	14.2	548	7.5	599	1.5	651	-	-
	20	19.6	365	18.5	416	13.0	467	6.2	519	-	-
	23	20.2	186	19.8	237	18.4	288	10.1	340	3.8	393
Isotensoid	14	9.4	641	3.2	692	-	-	-	-	-	-
	17	16.5	608	9.5	659	3.8	710	-	-	-	-
	20	19.0	568	16.4	619	8.7	671	3.1	723	-	-
	23	20.0	517	19.1	568	13.9	620	7.0	672	0.9	725
Tension Cone + Ringsail	14 / 20	15.1	546	12.6	597	8.4	648	3.5	700	-	-
	14 / 23	15.5	533	14.2	584	12.0	635	7.5	687	1.7	740
	14 / 26	15.6	518	14.8	569	13.6	620	10.8	672	5.2	725
	14 / 29	15.6	501	15.0	552	14.2	603	12.7	655	8.2	708
Isotensoid + Ringsail	14 / 20	13.6	600	11.6	651	8.3	702	3.5	755	-	-
	14 / 23	14.0	587	12.9	638	11.1	689	7.4	741	1.7	794
	14 / 26	14.1	572	13.4	622	12.3	674	10.2	726	5.2	779
	14 / 29	14.2	202	13.6	163	13.0	123	12.1	83	10.2	43

though much potential exists to improve the mass performance of the tension cone. Each of the decelerator systems were assessed based on two metrics – the mass of the IAD EDL system architecture relative to the reference DGB EDL system architecture, and the altitude at which propulsive descent can be initiated for each system. Systems that incorporated only a single IAD were favorable at higher terminal propulsion staging velocities while systems that incorporated a two-stage IAD-parachute system were more favorable at lower staging velocities. Because of their significant insensitivity to increased entry masses, IAD's can also increase payload mass considerably. Increasing the entry mass by 800 kg above the 4.2 MT DGB EDL architecture provided an increase in payload mass of approximately 600 kg, particularly when using smaller IAD's.

ACKNOWLEDGEMENTS

This work was funded by NASA Langley Research Center's Program to Advance Inflatable Decelerators for Atmospheric Entry (PAI-DAE). The authors would like to thank Dr. Juan R. Cruz of NASA Langley Research Center for his guidance on the structural aspects of IADs. We would also like to thank Jeff Tooley of the Jet Propulsion Laboratory for his assistance in developing the Mars 2016 entry trajectory model.

REFERENCES

[1] D. W. Way, R. W. Powell, A. Chen, A. D. Stelzner, A. M. San Martin, P. D. Burkhart, and G. F. Mendeck, "Mars Science Laboratory: Entry, Descent, and Landing System Performance," IEEEAC Paper 1467, 2006.

[2] R. D. Braun and R. M. Manning, "Mars Exploration Entry, Descent, and Landing Challenges," *Journal of Spacecraft and Rockets*, vol. 44, no. 2, pp. 310-323, March-April 2007.

[3] J. R. Cruz and J. S. Lingard, "Aerodynamic Decelerators for Planetary Exploration: Past, Present, and Future," AIAA 2006-6792, in *AIAA Guidance, Navigation, and Control Conference*, Keystone, CO, Aug. 21-24, 2006.

[4] A. Sengupta, et al, "Overview of the Mars Science Laboratory Parachute Decelerator System," AIAA 2007-2578, May 2007.

[5] M. S. Anderson, J. C. Robinson, H. G. Bush and R. W. Fralich, "A Tension Shell Structure for Application to Entry Vehicles," NASA TN D-2675, 1965.

[6] R. R. Barton, "Development of Attached Inflatable Decelerators for Supersonic Application," NASA CR-66613, 1968.

[7] "PEPP Ballute Design and Development Final Report," NASA CR-66585, 1967.

[8] L.W. Beegle, M. G. Wilson, F. Abillerira, J. F. Jordan, and G. R. Wilson, "A Concept for NASA's Mars 2016 Astrobiology Field Laboratory," *Astrobiology*, Vol. 7, No. 4, 2007, pp. 545-577.

[9] J. R. Cruz, A. D. Cianciolo, R. W. Powell, L. C. Simonsen, and R. H. Tolson, "Entry, Descent, and Landing Technology Concept Trade Study for Increasing Payload Mass to the Surface of Mars," *4th International Symposium on Atmospheric Reentry Vehicles and Systems*, Arachon, France, March 2005.

[10] N. E. Houtz, "Optimization of Inflatable Drag Devices by Isotensoid Design," AIAA Paper 64-437, July 1964.

[11] H. W. Bixby, E. G. Ewing, and T. W. Knacke, "Recovery Systems Design Guide," AFFDL-TR-78-151, 1978.

[12] M. M. Mikulas, Jr. and H. L. Bohon, "Development Status of Attached Inflatable Decelerators," *Journal of Spacecraft and Rockets*, vol. 6, no. 6, pp. 654-660, June 1969.

[13] W. D. Deveikis and J. W. Sawyer, "Aerodynamic Characteristics of Tension Shell Shapes at Mach 3.0," NASA TN D-3633, October 1966.

[14] J. Lee and S. M. Ruffin, "Parallel Computation of Solution Adaptive Cartesian Grids with SFC," AIAA Paper 2007-4088.

[15] W. C. Young and R. G. Budynas, Roark's Formulas for Stress and Strain, Chap. 12, New York: McGraw-Hill Professional, 7th Edition, 2001, pp. 526.

[16] A. C. Kyser, "Deployment Mechanics for an Inflatable Tension-Cone Decelerator," NASA CR-929, 1967.

[17] G. E. Weeks, "Buckling of a Pressurized Toroidal Ring Under Uniform External Loading," NASA TN D-4124, 1967.

[18] G. L. Brauer, D. E. Cornick, D. W. Olson, F. M. Petersen, and R. Stevenson, "Program to Optimize Simulated Trajectories (POST) Utilization Manual," MCR-87-583, NAS1-18147, 1987.

[19] M. S. Anderson, H. L. Bohon, and M. M. Mikulas, Jr., "A Structural Merit Function for Aerodynamic Decelerators," NASA TN D-5535, 1969.

[20] J. Stein and C. Sandy, "Recent Developments in Inflatable Airbag Impact Attenuation Systems for Mars Exploration," AIAA 2003-1900 in *44th AIAA/ASME/ASCE/AHS Structures, Structural Dynamics, and Materials Conference*, Norfolk,VA, Apr. 7-10, 2003.

[21] H. L. Bohon and R. Miserentino, "Deployment and Performance Characteristics of 5-Foot Diameter (1.5 m) Attached Inflatable Decelerators From Mach Number 2.2 to 4.4," NASA TN-D-5840, August 1970.

[22] G. L. Faurote, "Design, Fabrication, and Static Testing of Attached Inflatable Decelerator (AID) Models," NASA CR-111831, March 1971.

[23] J. Usry, "Performance of a Towed 48-Inch-Diameter (121.92-cm) Ballute Decelerator Testted in Free Flight at Mach Numbers From 4.2 to 0.4, " NASA TN-D-4943, February 1969.

[24] R. J. Mayhue and C. V. Eckstrom, "Flight-Test Results From Supersonic Deployment of an 18-Foot-Diameter (5.49-Meter) Towed Ballute Decelerator," NASA TM-X-1773, May 1969.

[25] W. A. Graham, "MK 82 Ballute Retarder System Updated for Advanced Weapons Program," AIAA 2001-2039, 2001.

[26] R. Humble, D. Lewis, W. Bissel and R. Sackheim, *Liquid Rocket Propulsion Systems*, 1st ed. New York: McGraw-Hill, 1995, pp. 272-279.

[27] D. W. Way, R. W. Powell, A. Chen, and A. D. Stelzner, "Asymptotic Parachute Performance Study," IEEEAC Paper 1465, 2006.

BIOGRAPHY

Ian Clark *is a PhD student at the Georgia Institute of Technology, where he also received his BS and MS. Ian's current research involves developing and maturing inflatable aerodynamic decelerators (IADs) for use during atmospheric entry. As part of this research, he has worked on conceptual IAD system design, entry flight mechanics trades, and the development of fluid-structure interaction codes capable of predicting the behavior of flexible decelerators. Presently, Ian is a research engineer on a series of supersonic wind tunnel tests of a candidate IAD configuration.*

Allison Hutchings *is a 1st-year graduate research assistant in the Space Systems Design Laboratory at the Georgia Institute of Technology. She has previously interned at Blue Origin. Allison's current focus is on structural analysis of entry systems. She has a B.S. in Engineering from Harvey Mudd College.*

Chris Tanner *is a 3rd-year graduate research assistant in the Space Systems Design Laboratory at the Georgia Institute of Technology. Chris has previously worked as a cooperative education student at NASA Johnson Space Center and as an intern at the Aerospace Corporation. He has participated in systems studies ranging from Mars surface systems to hypersonic airbreathing vehicles to Mars entry vehicles. His current research focuses on the experimental and computational analysis of inflatable aerodynamic decelerators. He has a BS and MS in Aerospace Engineering from Georgia Tech.*

Robert Braun *is an Associate Professor in the Guggenheim School of Aerospace Engineering at the Georgia Institute of Technology. As Director of Georgia Tech's Space Systems Design Laboratory, he leads a research program focused on the design of advanced flight systems and technologies for planetary exploration. He is responsible for undergraduate and graduate level instruction in the areas of space systems design, astrodynamics and planetary entry. Prior to coming to Georgia Tech, Dr. Braun worked at NASA Langley Research Center for sixteen years where he contributed to the design, development, test, and operation of several robotic space flight systems. Dr. Braun is an AIAA Fellow and the principal author or co-author of over 150 technical publications in the fields of planetary exploration, atmospheric entry, multidisciplinary design optimization, and systems engineering.*